ACS OMEGA

http://pubs.acs.org/journal/acsodf

Article

Research on the Influencing Factors and Prediction Model of Impact Airflow in the Process of Unloading of an Ore Pass Based on a Coupled Computational Fluid Dynamics and Discrete Element Method

Jiuzhu Wang, Cuifeng Du,* and YaPeng Wang

Cite This: *ACS Omega* 2021, 6, 23100–23109

Read Online

ACCESS | Metrics & More | Article Recommendations

ABSTRACT: In this paper, a coupled computational fluid dynamics and discrete element method (CFD-DEM) is used to numerically simulate the energy transfer of the ore falling process and the change law of impact airflow velocity under different influencing factors. The results are as follows: the total drag force is an important factor that determines the impact airflow velocity. The greater the total drag force, the greater the impact airflow velocity. The impact airflow velocity increases with the increase of mass flow rate and discharge height and decreases with the increase of ore size, and it is found that the discharge height has the greatest impact on the impact airflow velocity, the ore size is the second, and the mass flow rate is the smallest. Therefore, in the allowable range of mine production, the discharge height should be appropriately reduced. The mathematical model of the impact airflow velocity is obtained by multivariate nonlinear regression on the experimental results of orthogonal experiments.

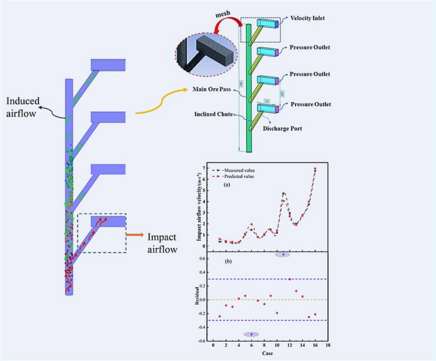

1. INTRODUCTION

With the increase of mining depth, ore pass transportation is widely used in China's metal mines due to its simple structure, convenient use, and cost-effectiveness. At the same time, the traffic of the ore pass increases with the increase of the degree of mechanization of the mine, which will inevitably make more mines to develop large-level and high ore pass systems. However, there are also some problems such as dust pollution to be solved in the transportation of the ore pass. When the ore moves in the ore pass, it will do work to the air, and form an impact airflow when the ore falls to the bottom of the ore pass, and impact airflow will cause dust pollution of the ore dumping chamber.

Hemeon[1] discussed the volumetric flow rate of air entrained when the material was in free fall and obtained the corresponding calculation expression. Morrison[2] thought that the volumetric flow rate of air entrainment is excessive as calculated by Hemeon's model and proposed a conservative equation. Tooker[3,4] also studied and revised the Hemeon model. Liu[5] studied the volumetric flow rate of air entrainment and found that the core of free falling particles contracted immediately after exit from the outlet of a hopper based on the Tooker model. Wypyc et al.[6] established a typical experimental system for measuring the volumetric flow rate of air entrainment but only studied the effect of drop height and product temperature on the entrained air and did not consider the effect of other factors on the volumetric flow rate of air entrainment. Arnold and Cooper[7] proposed a plume model to describe the complex air entrainment process of free-falling bulk materials. Plinke et al.[8] tested the dust production of titanium dioxide, limestone, glass beads, and lactose at different water contents, heights, particle size distributions, and material flows. Ogata et al.[9] studied the characteristics of powder jet through the free-fall experiment of glass beads. Uchiyama[10] conducted numerical simulation on the particle jet problem caused by solid particles falling into quiescent air from a slit orifice. Ansart et al.[11] have improved the Cooper experiments based on measuring entrained air, and they studied the airflow velocity distributions of falling powder by means of a particle image velocimetry system, and the results showed that the intensity and the vertical velocity fitted a Gaussian curve.[12,13] Esmaili et al.[14] studied the interaction between particles and air in free-falling of bulk materials through a series of computer simulations and experiments and measured the fluid velocity in the falling process of coarse materials using a particle image velocimetry

Received: May 8, 2021
Accepted: July 16, 2021
Published: August 31, 2021

technique, and the result of experiments was in good overall agreement with simulation results. Duan et al.[15] analyzed the correlation between the three factors of falling height, hopper outlet diameter and temperature of materials, and the dust generation rate of free-falling materials, and the research showed that the height of falling materials and the temperature had a great influence on the first fugitive dust rate, whereas the second fugitive dust rate is mainly decided by the hopper outlet diameter. Li et al.[16] studied the induced airflow velocity of falling materials in a semiclosed transfer station and discussed the nonlinear characteristics of induced airflow velocity with the mass flow, falling height, and the resistance coefficient of the shell. Li et al. also studied the airflow induced by regular particles in free fall through tubes,[17,18] Jalaal et al.[19] used a similar experimental device to Li's to study the influencing factors of induced airflow, and they considered all factors more fully. Chen et al.[20,21] studied the induced airflow and dust emission in the belt conveyor transfer by numerical simulation and proposed several scale models to reduce dust emission. Logachev also conducted a systematic study on the movement of airflow and particles in a closed chute.[22,23] He proposed a probabilistic approach for determining the drag of multiple falling particles of different sizes, instead of an empirically determined method for determining the drag coefficient of particles for a material moving in a chute.[24] He also devised a method to reduce the induced airflow in the enclosed chute.[25] Jaklič experimentally studied the separation of single-component powder particles with continuous particle size distribution. The study showed that particles with larger diameters aggregate at the bottom of the chute, while smaller particles are at the top of the chute.[26] Ma et al.[27] studied the dust pollution caused by air entrainment at the conveyor transfer points through experiments and numerical simulation and presented a new coal dust control program that was airtight negative pressure dust-control technology. Ullmann et al.[28,29] thoroughly studied the dust emission from belt conveyor transfer points and reviewed, compared and analyzed different calculation formulas and current design methods. Wang et al.[30,31] conducted an experimental study on the characteristics and dust generation rate of materials at different temperatures in the process of free falling, which showed that the first fugitive dust rate increased with the temperature increased. Wangchai et al. studied the experimental material flow and the subsequent discrete element method simulation in the rotating drum of two dustiness testers.[32]

At present, there are more studies on induced airflow at conveyor transfer points but fewer on impact airflow in the process of unloading at the discharge port.[33] The research on ore pass is mainly focused on the problem of hang-up in ore pass,[34−36] the prediction of lining wear life of bins and chutes, and so on.[37] Therefore, in this paper, CFD-DEM is used to simulate the impact airflow generated after ore unloading in the ore pass, and the influence of different factors on the impact airflow is analyzed to provide a theoretical basis for dust pollution prevention and control in the ore dumping chamber.

2. MECHANISM OF IMPACT AIRFLOW

The distribution of airflow in the ore pass will be changed after the ore falls from the discharge port, and the movement of the ore in the ore pass is similar to the piston motion. The area in front of the ore is a positive pressure area, while the static pressure behind the ore reduces and the dynamic pressure increases to form an induced airflow. When the ore falls into the ore bin, the pressurized air in front of the ore emerges from the ore dumping chamber, forming an impact airflow. The schematic diagram of the formation of the impact airflow is shown in Figure 1.

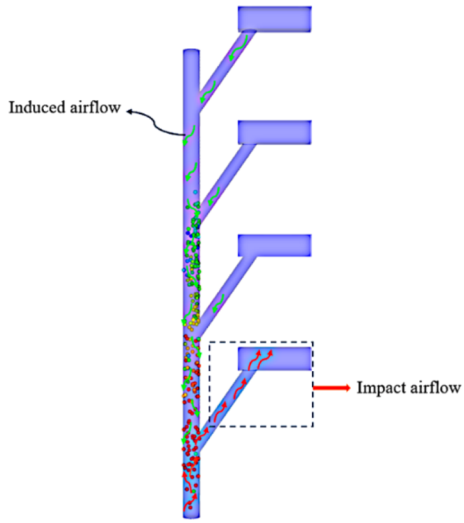

Figure 1. Schematic diagram of the formation of the impact airflow. From the perspective of energy conservation and transfer of the system, the potential energy of the ore is converted into the ore's kinetic energy, the kinetic energy of air, and the frictional dissipation of mechanical energy W_f, which can be described as eq 1.[28]

$$m_p g h = m_p \frac{u_p^2}{2} + m_a \frac{u_g^2}{2} + W_f \tag{1}$$

where m_p is the particle mass flow rate, kg/s; h is the particle fall height, m; u_p, u_g are the particle and air averaged velocities, m/s; m_a is the air mass flow rate, kg/s.

Assuming that the falling ores are spherical particles, the velocity of a single ore in the falling process can be calculated by eq 2:[38]

$$m_{p1} \frac{\mathrm{d}u_p}{\mathrm{d}t} = m_{p1} g - F_d - v_p \rho_g g \tag{2}$$

where m_{p1} is the particle mass, kg; v_p is the particle volume, m^3; ρ_g is the air density, kg/m^3. The last term in eq 2 represents the buoyancy force, and it is usually negligible for the large particle density relative to that of air. The drag force of a single particle can be calculated by formula 3:

$$F_d = 0.5 C_D \rho_g (u_g - u_p)^2 \frac{1}{4} \pi d_p^2 \tag{3}$$

where d_p is the ore diameter, m; C_D is the drag coefficient, which is related to Reynolds number.

From the interaction between ore and air, the drag force of the airflow is equal to the motion resistance of the ore. The work done to overcome the motion resistance in the falling process of the ore is the energy obtained by the air. If the resistance loss of air motion is not counted, the kinetic energy of the air is equal to the work done to overcome the motion resistance in the falling process of the ore. Therefore, we can obtain from eqs 1−3the magnitude of the impact airflow, which is related to the mass flow rate, discharge height, and ore size.

https://doi.org/10.1021/acsomega.1c02424
ACS Omega 2021, 6, 23100−23109

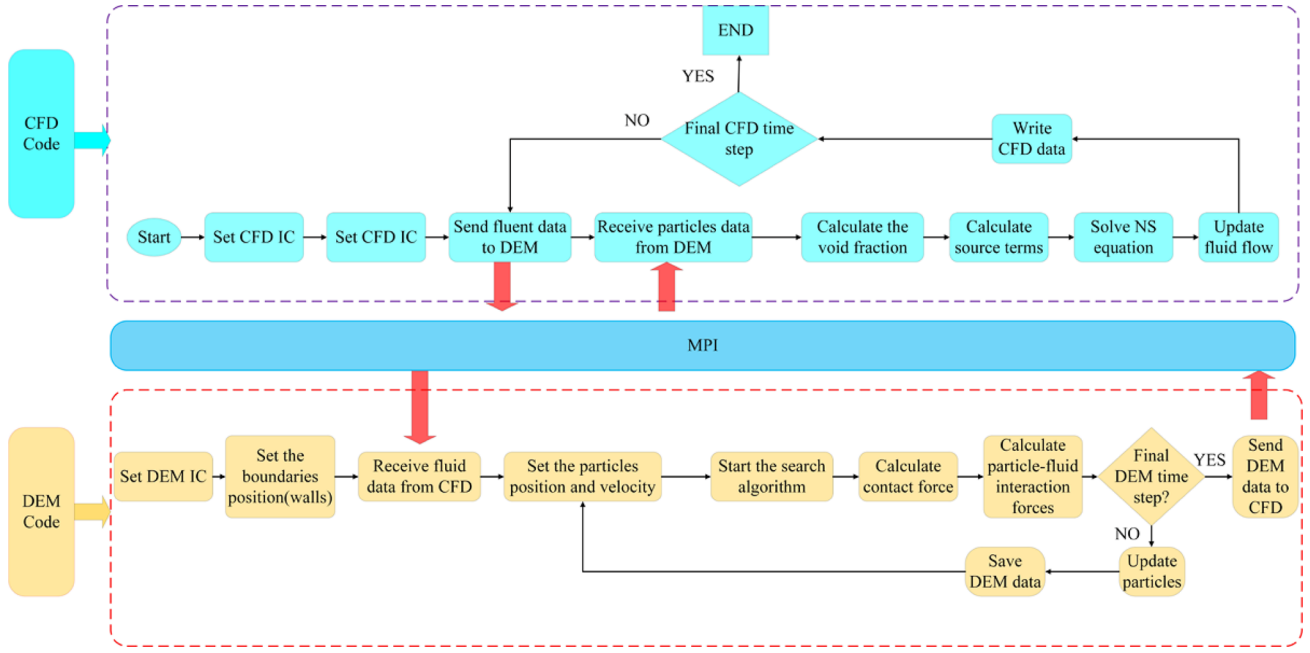

Figure 2. CFD-DEM model algorithm.

3. MATHEMATICAL MODEL AND PHYSICAL MODEL

3.1. CFD-DEM Coupled Mathematical Model. There are two CFD-DEM coupling models for particle flow and fluid coupling calculation: the Lagrangian model and the Eulerian model. The Lagrangian model only considers the momentum exchange between the liquid phase and the solid phase, which can be considered as the equivalent discrete phase model. The Eulerian model not only considers the momentum exchange between the fluid phase and the solid phase but also the effect of solid particles on the fluid phase, and the impact airflow is mainly caused by the movement of ore. Therefore, the Eulerian model in the CFD-DEM coupling model is suitable for simulating the generation of the impact airflow in the ore pass and the general algorithm of the CFD-DEM model,[39] as shown in Figure 2. The three-dimensional incompressible unsteady Navier−Stokes equation is chosen as the governing equation and the closed equations are established with the standard k-epsilon model. Only the momentum transfer is considered in the model, and thermal conduction is neglected. In the Cartesian coordinate system, the equations are as follows:[33,40]

Continuity equation:

$$\frac{\partial(\varepsilon\rho)}{\partial t} + \frac{\partial}{\partial x_i}(\varepsilon\rho u_i) = 0 \tag{4}$$

Momentum equation:

$$\frac{\partial}{\partial t}(\varepsilon\rho u_i) + \frac{\partial}{\partial x_j}(\varepsilon\rho u_i u_j) = -\frac{\partial \varepsilon p}{\partial x_i} + \frac{\partial \varepsilon \tau_{ij}}{\partial x_j} + \rho\varepsilon g_i - \sum F_{\mathrm{DEM}} \tag{5}$$

where ε_g denotes the local volume fraction of fluid in this system, ρ denotes the fluid density, with the unit kg/m^3; t denotes the time, with the unit s; x_i, x_j denotes the coordinates in the x-axis and y-axis directions, with the unit m; u_i, u_j denotes the fluid's velocity in the x-axis and y-axis directions, with the unit m/s; p denotes the effective turbulent pressure , with the unit Pa; g_i denotes the acceleration due to gravity , with the unit m/s^2; τ_{ij} denotes the tensor of stress; β denotes the interphase momentum exchange coefficient, with the unit $kg/m^3 \cdot s$; F_{DEM} denotes the drag force exerted by the particle within the fluid domain.

The turbulent kinetic energy and the turbulent pulsating dynamic energy dissipation rate equation can be written as[41,42]

$$\frac{\partial}{\partial t}(\rho k) + \frac{\partial}{\partial x_i}(\rho k u_i) = \frac{\partial}{\partial x_j}\left[\left(\mu + \frac{\mu_t}{\sigma_k}\right)\frac{\partial k}{\partial x_j}\right] + G_k - \rho\varepsilon + S_k \tag{6}$$

$$\frac{\partial}{\partial t}(\rho \varepsilon) + \frac{\partial}{\partial x_i}(\rho \varepsilon u_i) = \frac{\partial}{\partial x_j}\left[\left(\mu + \frac{\mu_t}{\sigma_\varepsilon}\right)\frac{\partial \varepsilon}{\partial x_j}\right] + \frac{\varepsilon}{k}C_{1\varepsilon}G_k - \frac{\varepsilon^2}{k}C_{2\varepsilon}\rho + S_\varepsilon \tag{7}$$

where $\mu_t = \rho C_\mu \frac{k^2}{\varepsilon}$; k denotes the fluid's turbulent kinetic energy, with the unit m^2/s^2; ε denotes the viscous dissipation induced by the vortex, with the unit m^2/s^3; G_k denotes the turbulent kinetic energy generated by the gradient of laminar velocity; S_k, S_ε denote the source items; μ denotes the laminar flow viscosity coefficient, with the unit $Pa \cdot s$; the values of $C_{1\varepsilon}$, $C_{2\varepsilon}$, C_μ, σ_ε, and σ_k are 1.44, 1.92, 0.09, 1.3, and 1.0, respectively.

The freestream drag model was chosen as the drag model of CFD-DEM coupling, which can be written as

$$F_d = 0.5 C_D \rho_g A |v| v \tag{8}$$

where $v = u_g - u_p$; A denotes the projected area of the particle, with the unit m^2.

The value of C_D in formula 9 depends on the Reynolds number, and the calculation formula of C_D under different Reynolds numbers can be written as[43,44]

https://doi.org/10.1021/acsomega.1c02424
ACS Omega 2021, 6, 23100−23109

$$C_D = \begin{cases} \dfrac{24}{Re} & Re \le 0.5 \\ \dfrac{24(1.0 + 0.25Re^{0.687})}{Re} & 0.5 < Re \le 1000 \\ 0.44 & Re \ge 1000 \end{cases} \quad (9)$$

where $Re = \frac{\alpha \rho_g d_p |v|}{\mu}$; α denotes the free volume of the CFD grid element.

3.2. Physical Model. A domestic ore pass was selected as a prototype: it serves four levels, with a height difference of 20 m between the levels, and is numbered one, two, three, and four from top to bottom. The height of the ore pass is about 90 m, with a 3.5 m diameter. The discharge port is 3 m in diameter. In addition, the length, width, and height of the ore dumping chamber are 20, 4, and 4.5 m, respectively. Solidworks was used to build a model as a 1:1 ratio, which was mainly composed of an ore dumping chamber, an inclined chute, and a main ore pass. The model is shown in Figure 3. Figure 4 shows the mesh quality

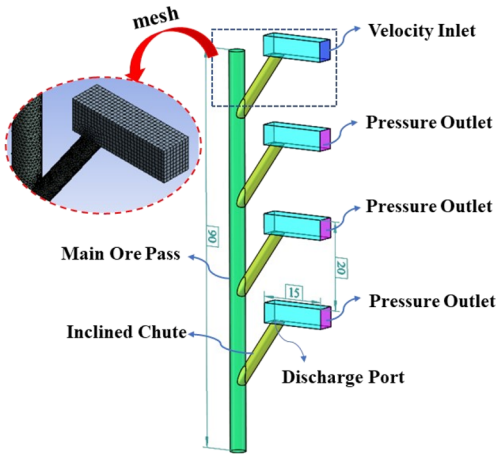

Figure 3. Physical model of ore pass.

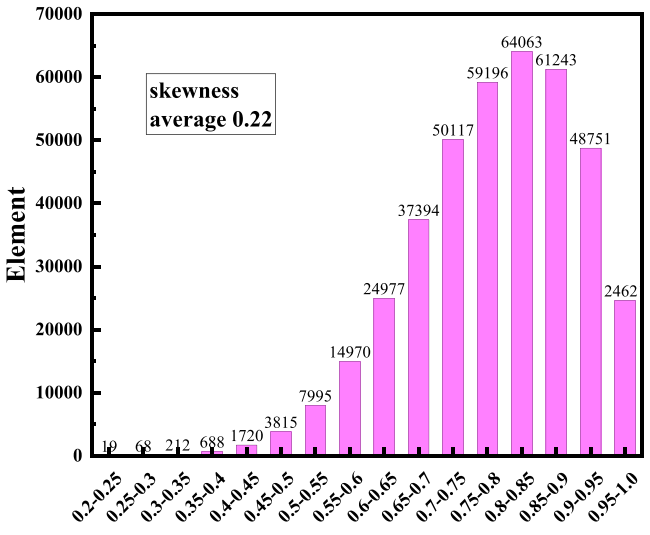

Figure 4. Mesh quality results.

of the ore pass, taking skewness as the evaluation index. The mesh quality is 0.22, which indicates that the mesh is good and meets the requirements of calculation.

3.3. Boundary Conditions. According to the field investigation, the primary unloading amount is about 4000 kg. The unloading time is 2 s, and the range of the ore size is from 0.05 to 0.2 m. The cross section of the first ore dumping chamber is selected as the velocity inlet, the other ore dumpling chamber are selected as the pressure outlet, and the rest of the model is set as the wall. At the same time, the discharge port in the fourth ore dumping chamber is set as a monitoring point to monitor the impact airflow velocity. Tables 1 and 2 list the settings of the main parameters in numerical simulation.

Table 1. Settings of Fluent Fluid Analysis Parameters

name	parameter	name	parameter
solver type	pressure-based	k-epsilon (2eqns)	standard
time	transient	turbulent intensity	3.4%
gravity	9.81 m/s^2	hydraulic diameter (m)	4.3
inlet boundary type	velocity inlet	wall	standard
outlet boundary type	pressure outlet	solution method	scheme (SIMPLE)

Table 2. Settings of EDEM Parameters

name	parameter	name	parameter
coupling method	Lagrangian	drag model	freestream equation
momentum under relaxation	0.7	volume under relaxation	0.7
particle density	4800 kg/m^3	particle contact model	Hertz–Mindlin model
particle diameter/m	0.05–0.2	factory type	dynamic
target mass	1000–4000 kg/s	total mass	4000 kg

4. RESULTS AND DISCUSSION

4.1. Model Reliability Verification. To verify the correctness of the simulation results, the simulation results are compared with the field results under a discharge height of 90 m, mass flow rate of 2000 kg/s, and ore size of 0.05 to 0.2 m, as shown in Figure 5. It can be shown from Figure 5 that the result of the field test is in good overall agreement with simulation results and the accuracy of simulation results is verified.

4.2. Analysis of Spatial and Temporal Distribution Characteristics of Airflow. In order to analyze the spatial and

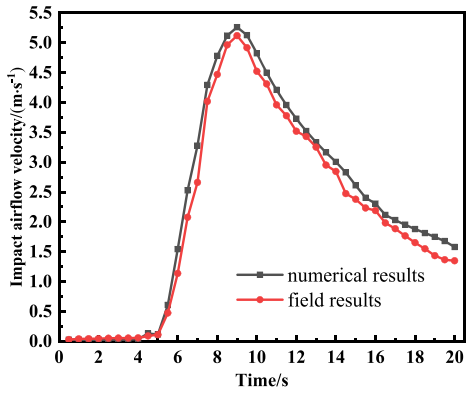

Figure 5. Comparison between simulation results and field test results.

https://doi.org/10.1021/acsomega.1c02424
ACS Omega 2021, 6, 23100−23109

temporal distribution characteristics of airflow in the ore pass after unloading, a numerical simulation was conducted with a discharge height of 90 m, ore size of 0.05 to 0.2 m, and mass flow rate of 2000 kg/s. Figure 6 shows the effect of ore movement on airflow distribution after unloading, and it can be seen from Figure 6a that the airflow behind the ore is severely disturbed at 3 s. The wind speed can reach 3.62 m/s. Furthermore, the distribution of airflow in other levels is not seriously affected, except the first level. Part of the ores reaches the ore storage bin at 4 s, and the airflow of the second, third, and fourth levels are also disturbed. Meanwhile, the airflow disturbance behind the ore is intensified, and the maximum velocity reaches 4.87 m/s. Within the time range from 5 to 8 s, most of the ores fall into the ore storage bin. The distribution of airflow in the first and the third levels changes less, while the distribution of airflow in the second and fourth levels changes more, as shown in Figure 6b,c.

Figure 7 shows the changing trend of impact airflow velocity with time. It can be seen from Figure 7 that when the ore size is constant, the impact airflow velocity increases first and then decreases with time. As the ore size changes, the smaller the ore size, the greater the impact airflow velocity and the time to reach the peak will be earlier.

4.3. Analysis of Energy Conversion in the Falling Process. A numerical simulation of energy conversion in the falling process was conducted with a discharge height of 90 m, ore size of 0.05 to 0.2 m, and mass flow rate of 2000 kg/s. It can be concluded from the formation mechanism of impact airflow that the drag force of ore affects the energy conversion during the falling of ore, so it is necessary to analyze the change trend of drag force. Taking ore sizes of 0.05, 0.10, 0.15 and 0.2 m as example, the magnitude of the drag force and energy conversion in the falling process are discussed. The variation law of the average drag force with different ore sizes is shown in Figure 8a. The average drag force first increases and then decreases with the increase of time. It reaches the maximum at 6 s, which can reach a maximum of 5.56 N, and the corresponding particle size is 0.20 m. Furthermore, the average drag force increases with the increase of ore size, which is consistent with formula 3. Figure 8b shows the relationship between the total drag force and time under different ore sizes. The trend of the total drag force with time is consistent with the average drag force, and the difference is that the total drag force gradually decreases with the increase of the ore size. The reason is as follows: when keeping the mass flow rate constant, the smaller the ore particle size, the larger the amount of ore per unit time, so the smaller degree of dispersion of ore in the ore pass, which increases the contact area between ore and air, as shown in Figure 8c. Hence, the total drag force increases.

Figure 9 shows the energy exchange of the ore at an ore size of 0.05 m, discharge height of 90 m, and mass flow rate of 2000 kg/s. It can be seen from Figure 9 that the potential energy of the ore gradually decreases and the kinetic energy gradually increases with the increase of time. At 6 s, the kinetic energy of the ore reaches the maximum, while at greater than 6 s, the kinetic energy of the ore gradually decreases. The maximum kinetic energy of the ore is 1600 kJ, and most of the potential energy is converted into kinetic energy of air.

4.4. Influence of Different Factors on the Impact Airflow. *4.4.1. Effect of Mass Flow Rate on Impact Airflow Velocity.* In the numerical simulation of the effect of mass flow rate on impact airflow, the setting range of each factor is as follows: the mass flow rate ranges from 1000 to 4000 kg/s, the ore size ranges from 0.05 to 0.2 m, and the discharge height is 90

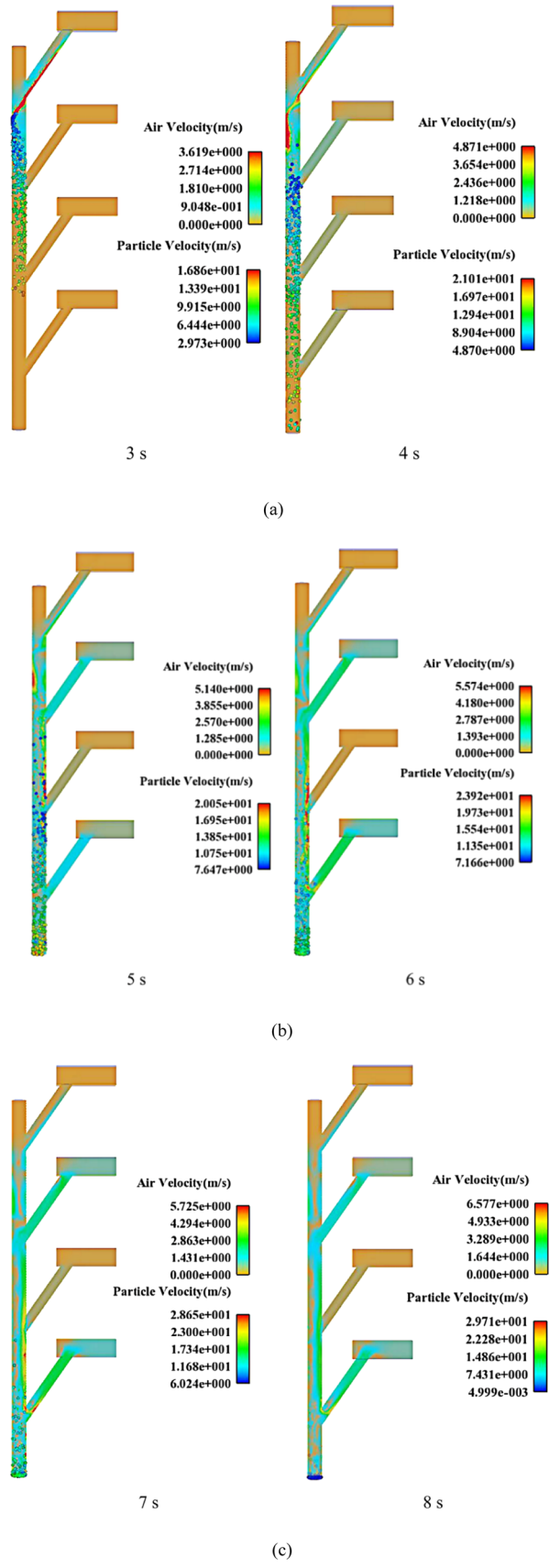

Figure 6. Spatial and temporal distribution of airflow and particle velocity: (a) 3−4 s, (b) 5−6 s, (c) 7−8 s.

https://doi.org/10.1021/acsomega.1c02424
ACS Omega 2021, 6, 23100−23109

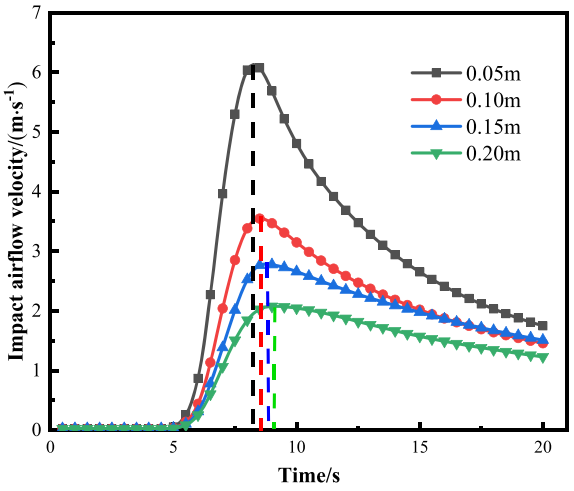

Figure 7. Relationship of impact airflow with time.

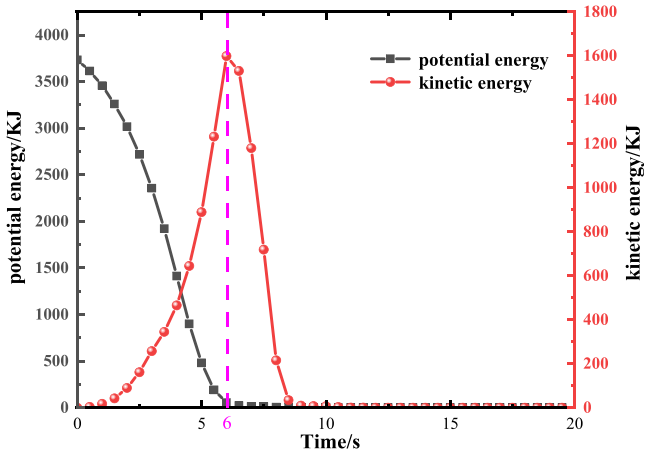

Figure 9. Energy exchange of the ore under different particle sizes.

m. Figure 10 shows the effect of mass flow rate on the total drag force. It can be observed that the total drag force increases with the increase of the mass flow rate when keeping the ore size constant. This is because the increase of the mass flow rate increases the amount of ore in the ore pass per unit time, which increases the contact area between ore and air, thus increasing the total drag force. Furthermore, when the mass flow rate is held constant, the total drag force increases with the ore size decreasing.

The variation of impact airflow velocity with mass flow rate is shown in Figure 11. The relationship between the impact airflow velocity and the mass flow rate is fit to a power function when the ore size remains constant, and the power exponents of a fitted curve decreases with the increase of ore size, which indicates that the increase rate of impact airflow velocity decreases with the increase of ore size. The reason for this phenomenon is as follows: it can be seen from Figure 10 that, with the increase of

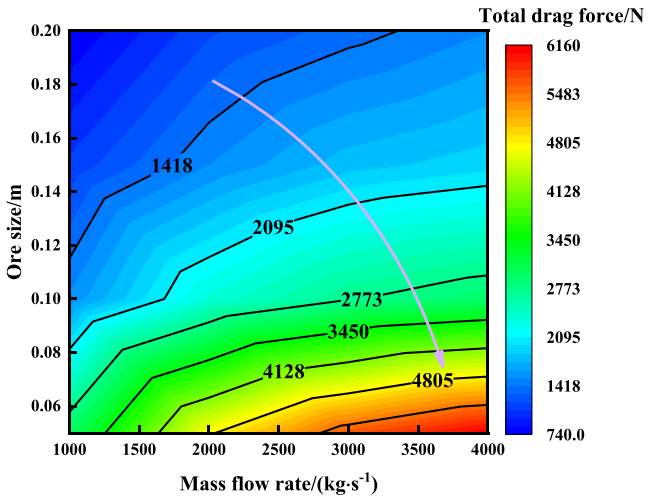

Figure 10. Effect of mass flow rate on total drag force.

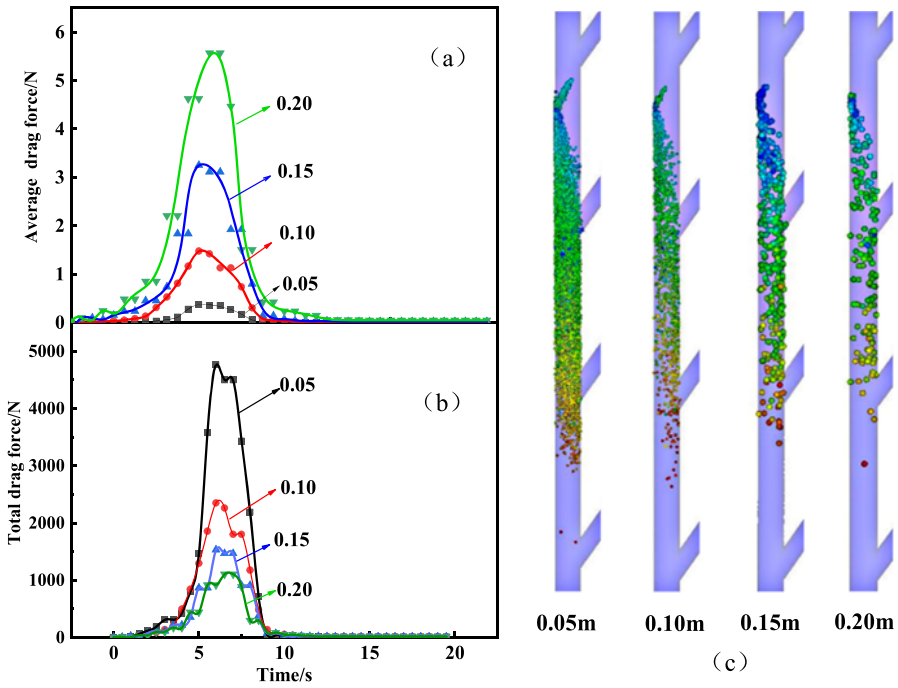

Figure 8. Relationship between the drag force and time: (a) average drag force, (b) total drag force, (c) degree of dispersion of ore in ore pass.

https://doi.org/10.1021/acsomega.1c02424
ACS Omega 2021, 6, 23100−23109

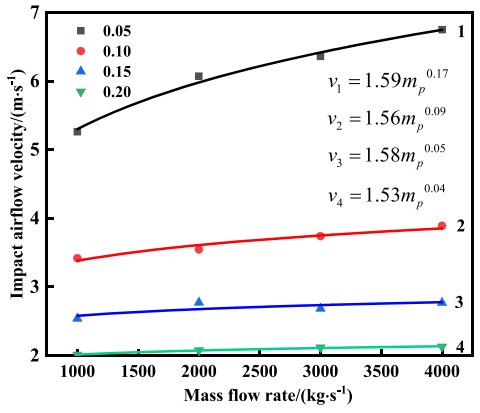

Figure 11. Effect of mass flow rate on impact airflow velocity.

ore size, the difference between the total drag force at different mass flow rates gradually decreases, which reduced the energy conversion between ore and air, thus reducing the increase rate of impact airflow velocity.

4.4.2. Effect of Discharge Height on Impact Airflow Velocity. A numerical simulation of the effect of discharge height on impact airflow was conducted with discharge heights of 30 to 90 m, mass flow rates of 1000 to 4000 kg/s, and ore size of 0.1 m. Figure 12 shows the variation trend of the total drag

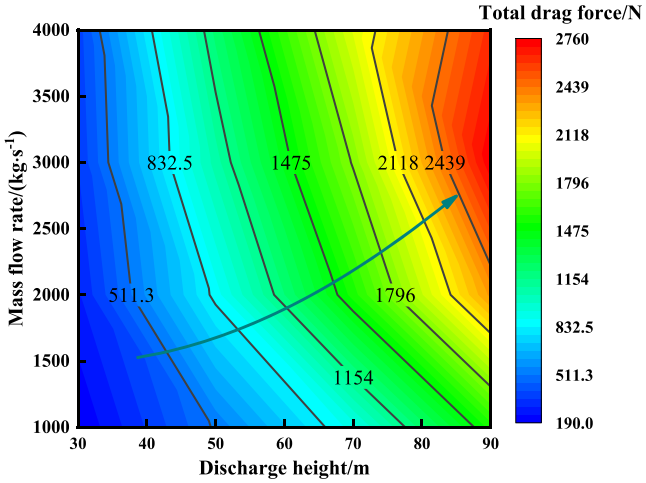

Figure 12. Variation trend of total drag force with discharge height.

force with discharge height. As can be seen from Figure 12, the total drag force increases with the increase of the discharge height when the mass flow remains unchanged. The main reason is that the potential energy of the ore increases with the increase of the discharge height, increasing the conversion between the ore's potential energy and the kinetic energy, and the relative speed of the ore and air also increases; therefore, the higher the discharge height, the greater the total drag force. Additionally, when the discharge height is kept the same, the total drag force increases with the increase of mass flow rate.

Figure 13 shows the effect of discharge height on the impact airflow velocity, the impact airflow velocity increases with the increase of the discharge height when the mass flow rate remains constant, and the total drag force increases with the increase of the discharge height, as shown in Figure 12, which increases the conversion between the ore and air. Therefore, the higher discharge height, the airflow obtains more energy and form and

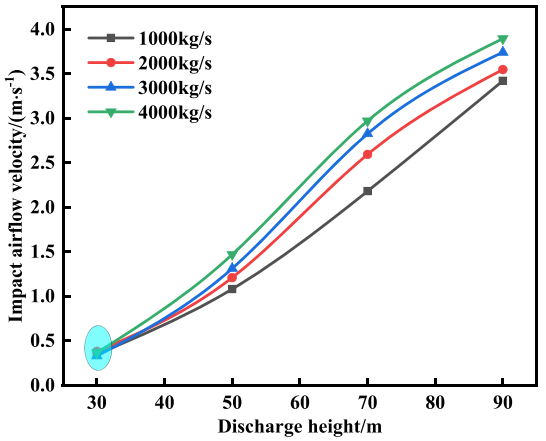

Figure 13. Effect of discharge height on the impact airflow velocity.

the greater the impact airflow velocity. Furthermore, when the discharge height is 30 m, the impact airflow velocity under each mass flow rate changes less, while when the unloading height is more than 30 m, the impact airflow velocity under each mass flow rate changes more, which is also determined by the total drag force.

4.4.3. Effect of Ore Size on Impact Airflow Velocity. A numerical simulation of the effect of ore size on impact airflow was conducted with ore sizes of 0.05 to 0.20 m, discharge heights of 30 to 90 m, and mass flow rate of 2000 kg/s. When the discharge height is held constant, the total drag force gradually decreases with the increase of the ore size, as shown in Figure 14.

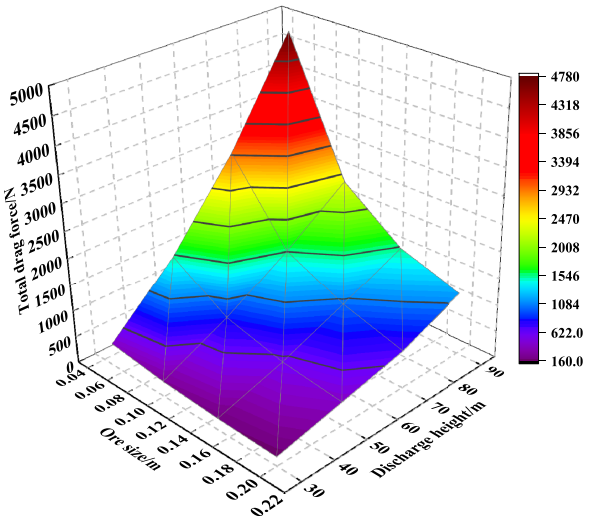

Figure 14. Variation trend of total drag force with ore size.

The reason is that the smaller particle size of the ore per unit volume makes a greater number of particles and increases the contact area between ore and air, so the total drag force increases with the decrease of ore size.

Figure 15 shows the effect of ore size on impact airflow velocity, and it can be seen from Figure 15 that the impact airflow velocity decreases with the increase of ore size. The reason may be as follows: upon further analysis, the smaller the ore particle size, the greater the drag force and the more energy exchanges between air and ore in the falling process, so the impact airflow velocity increases with the ore size decreasing. In

https://doi.org/10.1021/acsomega.1c02424
ACS Omega 2021, 6, 23100−23109

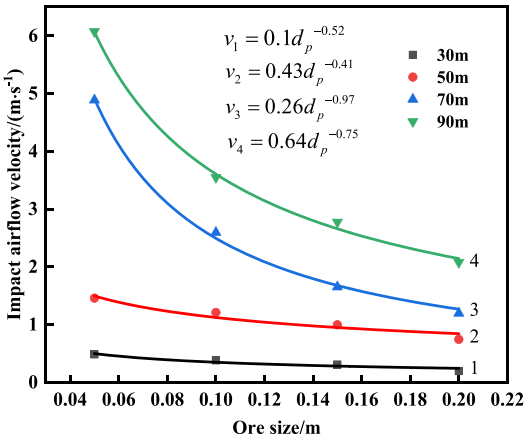

Figure 15. Effect of ore size on impact airflow velocity.

addition, the power exponents of a fitted curve ranged between −0.41 and −0.97.

4.5. Multiple Regression Analysis of Impact Airflow Velocity. Orthogonal experiments are a fast and economical experiment design method. The influence degree of the various factors on the impact airflow can be analyzed by the results of an orthogonal experiment. Therefore, the influence degree of different factors on impact airflow velocity was simulated by an orthogonal experiment, and the orthogonal experiment table and simulation results are shown in Table 3. The results of the orthogonal experiment were analyzed by the range analysis method, as shown in Table 4. The *K* value represents the average of the results using the same index at the same level, reflecting the difference of the results obtained by the same index at different levels. The *R* value denotes the range, which represents the difference between the maximum and minimum average values of the different levels at the same index and factor. By comparing the range value of different factors, it is found that the discharge height has the largest influence on the impact airflow velocity followed by the ore size, and the mass flow rate is the smallest.

Table 3. Orthogonal Test Results

case	discharge height	mass flow rate	ore size	impact airflow velocity
1	30	1000	0.05	0.397336
2	30	2000	0.1	0.380249
3	30	3000	0.15	0.280367
4	30	4000	0.2	0.350342
5	50	1000	0.1	1.080317
6	50	2000	0.05	1.456849
7	50	3000	0.2	0.807066
8	50	4000	0.15	1.006422
9	70	1000	0.15	1.501789
10	70	2000	0.2	1.195747
11	70	3000	0.05	4.718157
12	70	4000	0.1	2.96963
13	90	1000	0.2	2.012224
14	90	2000	0.15	2.774786
15	90	3000	0.1	3.740405
16	90	4000	0.05	6.750185

Table 4. Range Analysis of the Orthogonal Test

index		discharge height	mass flow rate	ore size
impact airflow velocity	K_1	0.352073	1.248	3.3306
	K_2	1.087664	1.452	2.043
	K_3	2.596331	2.387	1.391
	K_4	3.8194	2.769	1.091
	R	3.47	1.521	2.24

Upon further analysis, the variation of impact airflow velocity under different influence factors has non-linear characteristics. In order to intuitively represent the relationship between mass flow rate, discharge height, ore size, and impact airflow velocity, multivariate nonlinear regression analysis is conducted on the orthogonal experiment data, and the regression results were as follows:

$$v = 2.542e^{-5}h^{1.876}m_p^{0.237}d_p^{-0.705}(R^2 = 0.979) \quad (10)$$

where v denotes the impact airflow velocity, with the unit m/s; h denotes the discharge height, with the unit m; m_p denotes the mass flow rate, with the unit kg/s; d_p denotes the ore size, with the unit m; R^2 denotes the coefficient of determination.

Figure 16 shows the verification of regression model results. The coefficient of determination is 0.979, and the predicted value is in good agreement with the measured value. In addition, the residual values are between −0.6 and 0.7, and the residual values are closer to zero except case 6 and 11.

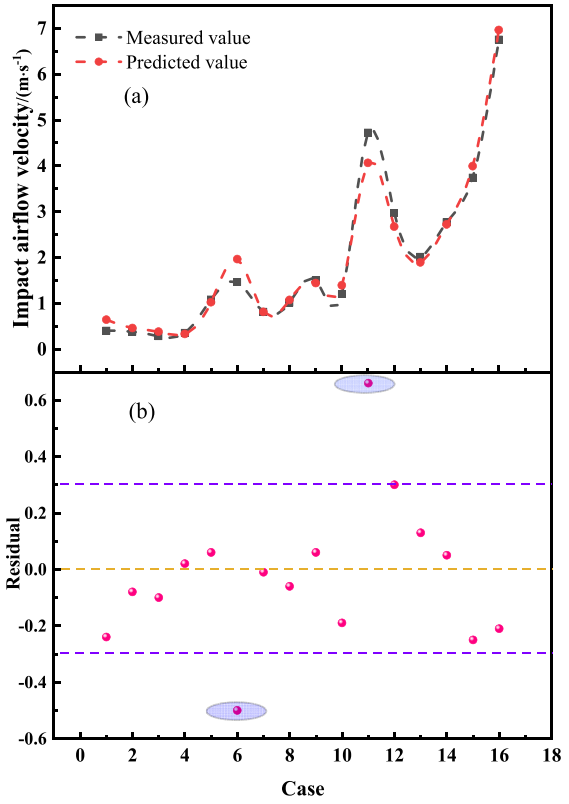

Figure 16. Verification of regression model results: (a) comparison of measured and predicted values and (b) residual.

5. CONCLUSIONS

(1) By analyzing the energy transfer of ores in the falling process and the formation mechanism of the impact airflow, it is found that the main influencing factors of impact airflow are mass flow rate, discharge height, and

https://doi.org/10.1021/acsomega.1c02424
ACS Omega 2021, 6, 23100−23109

ore size. The CFD-DEM coupling method is used to simulate the spatial and temporal distribution of the airflow and ore after unloading, the movement of ore changes the distribution of airflow in the ore pass, and the impact airflow is generated in the fourth ore dumping chamber at 6 s.

(2) The energy conversion during the ore falling process is analyzed, the potential energy of the ore is about 3700 kJ at 90 m, and the potential energy of the ore is gradually converted into kinetic energy of the ore and kinetic energy of air in the falling process. When the ore falls into the ore storage bin, the potential energy of the ore decreases to zero, and the kinetic energy increases to about 1600 kJ. Most of the potential energy is converted into kinetic energy of air.

(3) The influence of different factors on the impact airflow is mainly determined by the drag force. The greater the drag force, the more energy is transformed between the air and the ore and the greater the impact airflow velocity. The impact airflow velocity increases with increasing mass flow rate and discharge height and decreases with the increase of ore size. Therefore, the height of the ore pass should be reduced as much as possible in the mining design, and the mass flow rate and crushing degree of ore should be appropriately reduced in the mine production process.

(4) The results of the orthogonal experiment are analyzed by means of a range analysis method, and it is concluded that the discharge height has a greater influence on the impact airflow velocity followed by the ore size and the mass flow rate is the smallest. The theoretical formula of impact airflow velocity is obtained by multivariate nonlinear analysis.

AUTHOR INFORMATION

Corresponding Author

Cuifeng Du − *College of civil and resource engineering, University of Science and Technology Beijing, Beijing 100083, China; State Key Laboratory of High-Efficient Mining and Safety of Metal Mines, University of Science and Technology Beijing, Beijing 100083, China*; Email: ducuifeng@126.com

Authors

Jiuzhu Wang − *College of civil and resource engineering, University of Science and Technology Beijing, Beijing 100083, China; State Key Laboratory of High-Efficient Mining and Safety of Metal Mines, University of Science and Technology Beijing, Beijing 100083, China*; orcid.org/0000-0003-0184-9439

YaPeng Wang − *College of civil and resource engineering, University of Science and Technology Beijing, Beijing 100083, China; State Key Laboratory of High-Efficient Mining and Safety of Metal Mines, University of Science and Technology Beijing, Beijing 100083, China*; orcid.org/0000-0003-1849-972X

Complete contact information is available at: https://pubs.acs.org/10.1021/acsomega.1c02424

Notes

The authors declare no competing financial interest.

ACKNOWLEDGMENTS

Financial support from the National Key R&D Program of China (2018YFC0604605) and the Fundamental Research Fund for the Central Universities (FRF-TP-19-039A1) is gratefully acknowledged.

REFERENCES

(1) Hemeon, W. D. L. *Plant and Process Ventilation*; Industrial Press: New York, 1963; pp. 235−245.
(2) Morrison, J. N. Controlling dust emissions at belt conveyor transfer points, *Society of Mining Engineers.* AIME. 1971, *250*, 47−53.
(3) Tooker, G. E. Establishing design criteria for fugitive dust collection. *Bulk Solids Handl.* **1985**, *5*, 865−869.
(4) Tooker, G. E. Controlling fugitive dust emissions in material handling operations. *Bulk Solids Handl.* **1992**, *12*, 227−232.
(5) Liu, Z.; Wypych, P.; Cooper, P. Dust generation and air entrainment in bulk materials handling - a review. *Powder Handl. Process.* **1999**, *11*, 421−425.
(6) Wypyc, P.; Cook, D.; Cooper, P. Controlling dust emissions and explosion hazards in powder handling plants. *Chem. Eng. Process.: Process Intesif.* **2005**, *44*, 323−326.
(7) Cooper, P.; Arnold, P. Air entrainment and dust generation from a falling stream of bulk material. *Kona Powder Part. J.* **1995**, *13*, 125−134.
(8) Plinke, M. A. E.; Leith, D.; Boundy, M. G.; Lffler, F. Dust generation from handling powders in industry. *Am. Ind. Hyg. Assoc. J.* **1995**, *56*, 251−257.
(9) Ogata, K.; Funatsu, K.; Tomita, Y. Experimental investigation of a free falling powder jet and the air entrainment. *Powder Technol.* **2001**, *115*, 90−95.
(10) Uchiyama, T. Numerical analysis of particulate jet generated by free falling particles. *Powder Technol.* **2004**, *145*, 123−130.
(11) Ansart, R.; Ryck, A. D.; Dodds, J. A. Dust emission in powder handling: Free falling particle plume characterisation. *Chem. Eng. J.* **2009**, *152*, 415−420.
(12) Ansart, R.; De Ryck, A.; Dodds, J. A.; Roudet, M.; Fabre, D.; Charru, F. Dust emission by powder handling: Comparison between numerical analysis and experimental results. *Powder Technol.* **2009**, *190*, 274−281.
(13) Ansart, R.; Letourneau, J.; Ryck, A.; Dodds, J. A. Dust emission by powder handling: Influence of the hopper outlet on the dust plume. *Powder Technol.* **2011**, *212*, 418−424.
(14) Esmaili, A. A.; Donohue, T. J.; Wheeler, C. A.; Mcbride, W. M.; Roberts, A. W. On the analysis of a coarse particle free falling material stream. *Int. J. Miner. Process.* **2015**, *142*, 82−90.
(15) Duan, M.; Wang, Y.; Ren, X.; Qu, X.; Cao, Y.; Yang, Y.; Nian, L. Correlation analysis of three influencing factors and the dust production rate for a free-falling particle stream. *Particuology* **2017**, *34*, 126−133.
(16) Li, X.-C.; Li, Q.; Zhang, D.; Hu, Y.-F.; Xiong, J. J.; Luo, H. Q.; Jia, B. B.; Hu, H.-B. Nonlinear variation influence factors for induced airflow of bulk materials in transfer station. *Mater. Sci. Eng. Powder Metall.* **2014**, *19*, 508−513.
(17) Wang, D.; Li, X. Study of airflow induced by regular particles in freefall through tubes. *Adv. Powder Technol.* **2020**, *31*, 169−180.
(18) Li, X.; Li, Q.; Zhang, D.; Jia, B.; Luo, H.; Hu, Y. Model for induced airflow velocity of falling materials in semi-closed transfer station based on similitude theory. *Adv. Powder Technol.* **2015**, *26*, 236−243.
(19) Jalaal, M.; Ganji, D. D.; Ahmadi, G. Analytical investigation on acceleration motion of a vertically falling spherical particle in incompressible Newtonian media. *Adv. Powder Technol.* **2010**, *21*, 298−304.
(20) Chen, X. L.; Wheeler, C. A.; Donohue, T. J.; Mclean, R.; Roberts, A. W. Evaluation of dust emissions from conveyor transfer chutes using experimental and CFD simulation. *Int. J. Miner. Process.* **2012**, 101−108.

(21) Chen, X.; Wheeler, C. Computational Fluid Dynamics (CFD) modelling of transfer chutes: A study of the influence of model parameters. *Chem. Eng. Sci.* **2013**, *95*, 194−202.
(22) Logachev, I. N.; Logachev, K. I. *Industrial Air Quality and Ventilation: Controlling Dust Emissions*; CRC Press: Boca Raton, 2014; pp1−379.
(23) Logachev, I. N.; Logachev, K. I.; Averkova, O. A. *Local Exhaust Ventilation: Aerodynamic Processes and Calculations of Dust Emissions*; CRC Press: Boca Raton, 2015; pp. 385−529.
(24) Logachev, I. N.; Popov, E. N.; Logachev, K. I.; Averkova, O. A. Refining the method for determining the flow rate of air entrained by freely falling polydisperse loose material. *Powder Technol.* **2020**, *373*, 323.
(25) Logachev, I. N.; Logachev, K. I.; Averkova, O. A. Methods and Means of Reducing the Power Requirements of Ventilation Systems in the Transfer of Free-Flowing Materials. *Refract. Ind. Ceram.* **2013**, *54*, 258−262.
(26) Jaklič, M.; Kočevar, K.; Srčič, S.; Dreu, R. Particle size-based segregation of pharmaceutical powders in a vertical chute with a closed bottom: An experimental evaluation. *Powder Technol.* **2015**, *278*, 171−180.
(27) Ma, Y.; Jia, H.; Zhang, D. Airtight negative pressure dust-control technology and application of transpersite in the coal conveyer belt system. *J. Coal Sci. Eng. (China)* **2008**, *14*, 562−566.
(28) Ullmann, A.; Dayan, A. Exhaust volume model for dust emission control of belt conveyor transfer points. *Powder Technol.* **1998**, *96*, 139−147.
(29) Li, X. C.; Wang, Q. L.; Liu, Q.; Hu, Y. F. Developments in studies of air entrained by falling bulk materials. *Powder Technol.* **2016**, *291*, 159−169.
(30) Wang, Y.; Duan, M.; Ren, X.; Qu, X.; Cao, Y.; Yang, Y.; Fan, H.; Chu, Z. Experimental study of dust emission: Comparison between high-temperature and ambient-temperature materials. *Powder Technol.* **2016**, *301*, 1321−1329.
(31) Wang, Y.; Ren, X.; Zhao, J.; Chu, Z.; Cao, Y.; Yang, Y.; Duan, M.; Fan, H.; Qu, X. Experimental study of flow regimes and dust emission in a free falling particle stream. *Powder Technol.* **2016**, *292*, 14−22.
(32) Wangchai, S.; Hastie, D. B.; Wypych, P. W. The investigation of particle flow mechanisms of bulk materials in dustiness testers. *Part. Sci. Technol.* **2015**, *34*, 241−254.
(33) Wang, Y.; Jiang, Z.; Chen, J.; Chen, J.; Wang, M. Study of high-pressure air curtain and combined dedusting of gas water spray in multilevel ore pass based on CFD-DEM. *Adv. Powder Technol.* **2019**, *30*, 1789−1804.
(34) Vo, T.; Yang, H.; Russell, A. R. Cohesion and suction induced hang-up in ore passes. *International Journal of Rock Mechanics and Mining Sciences.* **2016**, *87*, 113−128.
(35) Remennikov, A. M.; Mutton, V.; Nimbalkar, S.; Ren, T. Experimental and numerical investigation of high-yield grout ore pass plugs to resist impact loads. *International Journal of Rock Mechanics and Mining Sciences.* **2014**, *70*, 1−15.
(36) Hadjigeorgiou, J.; Lessard, J. F. Numerical investigations of ore pass hang-up phenomena. *International Journal of Rock Mechanics and Mining Sciences.* **2007**, *44*, 820−834.
(37) Roberts, A. W.; Wiche, S. J. Prediction of lining wear life of bins and chutes in bulk solids handling operations. *Tribol. Int.* **1993**, *26*, 345−351.
(38) Zhu, H. P.; Zhou, Z. Y.; Yang, R. Y.; Yu, A. B. Discrete particle simulation of particulate systems: Theoretical developments. *Chem. Eng. Sci.* **2007**, *62*, 3378−3396.
(39) Farivar, F.; Zhang, H.; Tian, Z. F.; Gupte, A. CFD-DEM simulation of fluidization of multisphere- modelled cylindrical particles. *Powder Technol.* **2020**, *360*, 1017−1027.
(40) Wang, Z.; Teng, Y.; Liu, M. A semi-resolved CFD−DEM approach for particulate flows with kernel based approximation and Hilbert curve based searching strategy. *J. Comput. Phys.* **2019**, *384*, 151−169.
(41) van der Hoef, M.; Annaland, M.; Kuipers, J. Computational fluid dynamics for dense gas−solid fluidized beds: a multi-scale modeling strategy. *Chem. Eng. Sci.* **2004**, *59*, 5157−5165.
(42) van der Hoef, M. A.; van Annaland, M.; Kuipers, J. A. M. Computational fluid dynamics for dense gas-solid fluidized beds: a multi-scale modeling strategy. *China Particuol.* **2005**, *3*, 69−77.
(43) Oesterlé, B.; Dinh, T. B. Experiments on the lift of a spinning sphere in a range of intermediate Reynolds numbers. *Exp. Fluids* **1998**, *25*, 16−22.
(44) Hu, G. M. *Analysis and Simulation of Particle System by Discrete Element Method: Industrial Application of Discrete Element Method and Introduction to EDEM Software*; Wuhan University of Technology Press: Hubei (in China), 2010; pp. 139−163.

https://doi.org/10.1021/acsomega.1c02424
ACS Omega 2021, 6, 23100−23109